PAPER

Rational design of M−N$_4$−Gr/V$_2$C heterostructures as highly active ORR catalysts: a density functional theory study†

Yunjian Chen,[ab] Qi Jiang,[ab] Xue Bai,[ab] Pengyue Shan,[ab] Tong Liu,[ab] Yazhou Wang, [iD][ab] Hong Cui, [iD] *[ab] Rong Feng,[ab] Qin Kang,[ab] Zhiyong Liang[ab] and Hongkuan Yuan [iD][c]

Inspired by the composites of N-doped graphene and transition metal-based materials as well as MXene-based materials, heterostructures (M−N$_4$−Gr/V$_2$C) of eight different transition metals (M = Ti, Cr, Mn, Fe, Co, Ni, Cu, and Zn) doped with nitrogen-coordinated graphene and V$_2$C as potential catalysts for the oxygen reduction reaction (ORR) using density functional theory (DFT) were designed and are described herein. The calculations showed that the heterostructure catalysts (except for Zn−N$_4$−Gr/V$_2$C) were thermodynamically stable. Ni−N$_4$−Gr/V$_2$C and Co−N$_4$−Gr/V$_2$C showed higher activities towards the ORR, with overpotentials as low as 0.32 and 0.45 V, respectively. Excellent catalytic performance results were observed from the change in electronic structure caused by the strong interaction between V$_2$C and the graphene layers as well as the synergistic effect between the MN$_4$ groups and the graphene layers. This study further provides insights into the practical application of ORR catalysts for MXene systems through the modulation of the electronic structure of two-dimensional materials.

1 Introduction

In recent years, the development and utilization of clean energy have received global attention due to the serious environmental pollution caused by fossil fuels. Proton exchange membrane fuel cells (PEMFCs), as clean and efficient energy conversion devices, have attracted increasing attention due to their high energy transformation efficiency, high power density, and low emissions.[1,2] The cathode oxygen reduction reaction (ORR) is key to determining the fuel cell performance and energy transfer efficiency of PEMFCs, and the slow dynamics process is a major limiting factor in their efficiency.[3,4] Currently, the most widely used cathode catalysts in PEMFCs are Pt/C catalysts,[5] but their high cost, low stability, and low activity hinder their large-scale commercialization. Therefore, to reduce the use of Pt metals, noble metal-free catalysts should be screened and designed for the ORR.

Two-dimensional (2D) transition metal carbides and nitrides, known as MXenes, constitute a large family of 2D materials.[6] To date, MXenes have attracted significant attention for their potential applications in energy storage,[7] sensors,[8–10] and catalysis.[11–13] Specifically, MXenes with fast charge transfer properties, adjustable chemical-specific surface area, and high electrical conductivity offer broad prospects for electrochemical energy applications. They are also considered as promising carriers and prominent conductivity enhancers to obtain synergistic effects for fast charge transfer kinetics.[14,15] Zhu *et al.*, have synthesized superlattice-like heterostructure of Fe–N–C with MXene by experiments with a positive onset potential of 0.92 V in the electrocatalytic oxygen reduction reaction (ORR) and a durability of 20 h in alkaline electrolytes.[16] Zhang *et al.*, obtained Ni1/Ni2- and Fe1/Ni2-modified MXene-based double atom catalysts (DACs) as excellent bifunctional ORR/OER catalysts by introducing non-precious metals such as Fe/Co/Ni on the MXene surface through first-principles calculations.[17] Zhou *et al.*, by first-principles calculations for 3d, 4d and 5d transition metal single atoms immobilized on the surface of 2D titanium carbides (Ti$_2$CT and Ti$_3$C$_2$T) as active sites, derived good ORR activity for single-atom Cu-doped Ti$_2$CO$_2$ catalysts with an overpotential of 0.25 V.[18] V$_2$C exhibited good performance as a carrier material for catalysts in the ORR.

Nitrogen atom-doped graphene[19–21] is a potential alternative to Pt-based catalysts due to its high activity and low cost. To design highly stable catalysts, they must be stabilized using novel supports. 2D MXenes with abundant nonmetallic groups include a graphene layer stabilized by the strong interaction forces of nitrogen coordination, which not only modulates the catalytic properties of the selected transition metals but also affects the intrinsic activity of the 2D MXenes.[22–25] Constructing

School of Mechanical Engineering, Shaanxi University of Technology, Hanzhong, Shaanxi, 723001, China. E-mail: hongcui@snut.edu.cn

bShaanxi Key Laboratory of Industrial Automation, Shaanxi University of Technology, Hanzhong, Shaanxi, 723001, China

cSchool of Physical Science and Technology, Southwest University, Chongqing, 400715, China

heterogeneous structures is a powerful strategy for designing high-performance materials, where phenomena such as charge transfer can be observed.[26,27] Geng *et al.* synthesized a large-area Mo_2C/MXene on graphene templates,[28] and this heterogeneous structure was highly active for electrocatalysis *via* the hydrogen evolution reaction (HER) with a lower starting voltage than that of Mo_2C-only electrodes. Zhou *et al.* constructed G/Ti_2C, G/V_2C, G/Nb_2C, and G/Mo_2C heterostructures by theoretical simulations, among which G/V_2C and G/Mo_2C readily underwent electrocatalysis with an ORR overpotential of 0.36 V.[29]

Using their synergistic effects, the composites of N-doped graphene and transition metal-based materials are one of the main electrocatalysts for HER, OER, and ORR.[30–32] Due to the excellent conductivity and charge transfer kinetics of V_2C MXene,[9,33,34] We are inspired to investigate the possibility of using it as a potential carrier material for N-doped graphene to develop efficient ORR catalysts. Considering the nature of transition metals and the effective charge transfer kinetics of MXene, the heterostructure of N-doped graphene and transition metal-based material composites with V_2C ($M–N_4–Gr/V_2C$) were investigated as a superior ORR catalyst. The electrocatalytic properties of eight different transition metals (M = Ti, Cr, Mn, Fe, Co, Ni, Cu, and Zn) doped with nitrogen ligands were investigated for graphene with V_2C heterostructures. Their electronic properties, free energies, and volcano curves were obtained using DFT calculations. The calculations showed that the MN_4 group was the active center of the reaction intermediate and $Ni–N_4–Gr/V_2C$ had a promising ORR catalytic effect. The ORR effect of the eight catalysts was investigated by analyzing the interactions between the MN_4 groups and the V_2C substrates through the charge transfer mechanism. The density of states (DOS) indicated that increased ORR activity arose from the moderate hybridization between the d-orbital of the Ni atom and the p-orbital of O. The volcano curves indicate that $Ni–N_4–Gr/V_2C$ and $Co–N_4–Gr/V_2C$ are located at the peak of the volcano, resulting in the highest activity with moderate interaction between the reaction intermediate and the catalyst. This study provides a novel approach for the design of ORR catalysts through the modulation of the electronic structure of 2D MXene materials and inspiration for the practical application of high-performance electrocatalysts in MXene systems.

2 Calculation method

2.1 Method

All calculations were performed using the Vienna *Ab initio* Simulation Package (VASP),[35] wherein the Perdew–Burke–Ernzerhof (PBE) generalization of the generalized gradient approximation (GGA) was used to describe the exchange relation effect.[36] A plane-wave basis set with a cutoff energy of 550 eV and a projector-augmented wave (PAW) potential were used.[37] To simulate the heterogeneous structure of graphene and MXene, we used $2 \times 2 \times 1$ graphene supercell and $1 \times 3 \times 1$ V_2C supercell while swapping the *a* and *b* coordinates of graphene. Specifically, the lattice mismatch ratio is 1.85% (Table 1). The initial layer spacing of the heterogeneous structure was set to 3 Å. A vacuum layer of 20 Å was applied in the

Table 1 Lattice mismatch ratio (δ) and interlayer distance (*d*) of the graphene/MXene heterostructures

System	*a* (Å)	*b* (Å)	Heterostructure (Å)	δ (%)	*d* (Å)
G	2.46	4.26	4.92×8.52 (2×2)	1.85%	2.10
V_2C	5.01	2.89	5.01×8.67 (1×3)		

vertical direction so that the lattice strain of graphene has a negligible effect on the binding properties and catalytic activity.[15] The model structure is fully optimized in the constrained supercell using a total energy of 10^{-4} eV and a force of 0.02 eV Å^{-1}. The weak van der Waals (vdW) interactions between the graphene layers and MXene can be described using Grimme's DFT-D3 dispersion correction scheme.[38] The Gamma scheme was used to sample the Brillouin zone, with a *k*-point grid of $2 \times 3 \times 1$ for geometric optimization and $4 \times 6 \times 1$ for electronic structure calculations. The partial charge density and charge transfer were evaluated by Bader charge analysis.[39] The DOS was calculated to analyze the atomic bonding, interatomic interactions, and electrical conductivity in the reaction following adsorption. The minimum energy pathway was obtained using the climbing image nudged elastic band method[40] and MD simulations with a time step of 2 fs using density functional tight-binding.[41]

2.2 Calculations

The adsorption energies (E_{ads}) were calculated for all intermediates during the ORR reactions (*O, *O_2, *OH, and *OOH):

$$E_{ads} = E_{ad/S} - E_{ad} - E_S \tag{1}$$

where $E_{ad/S}$, E_{ad}, and E_S represent the energies of the MXene substrate, free adsorbate, and adsorbate on the pure MXene substrate, respectively. A negative E_{ads} indicates that the adsorbed molecules are energetically favored to adsorb on the catalyst surface.

The free energy diagram of the reaction was calculated according to the method developed by Nørskov *et al.* The reaction free energy is the difference between the initial and final states, and the change in the Gibbs free energy at each step of the ORR is given by:
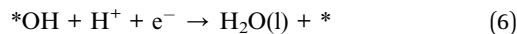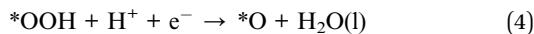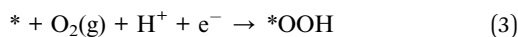
$$\Delta G = \Delta E_{DFT} + \Delta ZPE - T\Delta S + \Delta G_U + \Delta G_{pH} \tag{2}$$

where ΔE_{DFT}, ΔZPE, and ΔS are the changes in the reaction energy, zero-point energy, and entropy from the initial state to the final state, respectively, as calculated by DFT. *T* is the standard room temperature (298.15 K). The vibrational frequencies were calculated by density general function theory, and the ZPE correction values and entropies were obtained. The vibrational frequencies and entropies of the gas-phase molecules can be found in the NIST database.[42] ΔG_U is the free energy contribution associated with the applied electrode potential U, while ΔG_{pH} is the correction for the H^+ free energy by concentration. $\Delta G_{pH} = \ln 10 \times pH \times k_B T$, where k_B is the Boltzmann constant, and pH = 0 under acidic conditions. The standard

Table 2 Gibbs free energy of oxygen-containing intermediates (O, OH, and OOH) ΔG_{*O}, ΔG_{*OH}, and ΔG_{*OOH}; η^{*ORR} represents the overpotential in the ORR process

System	ΔG_{*O}	ΔG_{*OH}	ΔG_{*OOH}	η^{*ORR}
Ti–N$_4$–Gr/V$_2$C	−1.67	−1.49	2.01	—
Cr–N$_4$–Gr/V$_2$C	−0.01	−0.22	2.94	1.45
Mn–N$_4$–Gr/V$_2$C	1.10	0.19	3.31	0.98
Fe–N$_4$–Gr/V$_2$C	1.65	0.54	3.54	0.69
Co–N$_4$–Gr/V$_2$C	2.26	0.78	3.80	0.45
Ni–N$_4$–Gr/V$_2$C	2.75	0.91	3.96	0.32
Cu–N$_4$–Gr/V$_2$C	2.73	0.73	3.84	0.50

Fig. 1 (a) Top view and (b) side view of M-doped N-coordinated graphene supported by V$_2$C/MXene, and their interlayer distances; the pink, cyan, and gray balls denote V, N, and C atoms, respectively.

hydrogen electrode (SHE) method was used to calculate the ORR overpotential (η^{*ORR}), and we considered the 4e$^-$ associate pathway of the ORR under acidic conditions, which is the main mechanism of transition metal-doped graphene with V$_2$C/MXene heterostructured catalysts.

$$* + O_2(g) + H^+ + e^- \rightarrow *OOH \qquad (3)$$

$$*OOH + H^+ + e^- \rightarrow *O + H_2O(l) \qquad (4)$$

$$*O + H^+ + e^- \rightarrow *OH \qquad (5)$$

$$*OH + H^+ + e^- \rightarrow H_2O(l) + * \qquad (6)$$

where * represents the adsorption sites on the catalyst surface and *OOH, *O, and *OH are oxygen intermediates. The Gibbs free energy was calculated for each ORR step (Table 2), and the ORR overpotential is given by:

$$\eta_{ORR} = 1.23 - \Delta G_{min}/e \qquad (7)$$

where ΔG_{min} is the minimum Gibbs free energy for the four reaction steps given by eqn (3)–(6) and 1.23 V is the equilibrium potential of water at pH 0 and 298.15 K.
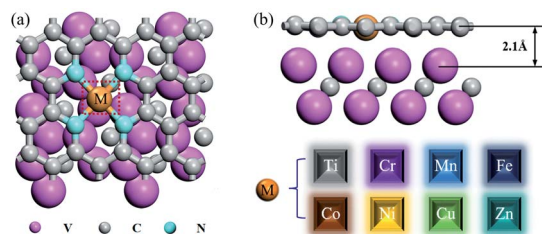
The expression was used to calculate the formation energy of the M–N$_4$–Gr/V$_2$C defect E_f:

$$E_f = E_{M-N_4-C/V_2C} + 6\mu_C - (E_{g/V_2C} + 4\mu_N + \mu_M) \qquad (8)$$

where E_{M-N_4-Gr/V_2C} and E_{g/V_2C} are the respective energies with M–N$_4$–Gr/V$_2$C and g/V$_2$C defects within the optimized geometry of graphene; the numbers 4 and 6 denote the number of doped N and C atoms removed from the pristine graphene sheet to form M–N$_4$–Gr defects; μ_C is the chemical potential of carbon as the total energy per carbon atom of defect-free graphene;[39,43] μ_N is the chemical potential of N or half of the total energy of a N$_2$ molecule; and μ_M is the chemical potential of an isolated transition metal atom.

2.3   Models

In this study, the heterostructure formed by transition metal-doped graphene with V$_2$C was used to improve the activity of the cathode catalyst. Four N atoms were chosen to modify graphene, and the transition metal atoms were placed in the center of the N atoms, resulting in an M–N$_4$–Gr/V$_2$C heterostructure. A total of eight structures were studied: Ti–N$_4$–Gr/V$_2$C, Cr–N$_4$–Gr/V$_2$C, Mn–N$_4$–Gr/V$_2$C, Fe–N$_4$–Gr/V$_2$C, Co–N$_4$–Gr/V$_2$C, Ni–N$_4$–Gr/V$_2$C, Cu–N$_4$–Gr/V$_2$C, and Zn–N$_4$–Gr/V$_2$C (Fig. 1a).

3   Results and discussion

Composites of N-doped graphene and transition metal-based materials that form heterostructures with MXene are known to act as bifunctional catalysts for ORR and OER.[14] To further motivate the catalytic activity of single atom-doped N-liganded graphene as an active site, we formed heterostructures of M-doped N-liganded graphene with V$_2$C. The synthesis of such heterostructures is feasible, as recent experiments generated MoC$_2$ films directly on the graphene surface via chemical deposition as well as on the graphene nanoribbons.[24] The distance between our designed graphene and V$_2$C heterostructure is 2.1 Å (Fig. 1b) and resulted in an energy of −10.13 eV, indicating strong coupling between the interfaces. After the transition metal was modified, the formation energy was calculated (shown in Fig. 2), where a negative value indicated the greater stability of the structure, and only the Zn-doped N-liganded graphene heterostructure was found to be unstable. The other transition metals follow the sequence according to stability intensity: Ti–N$_4$–Gr/V$_2$C > Co–N$_4$–Gr/V$_2$C > Fe–N$_4$–Gr/V$_2$C > Ni–N$_4$–Gr/V$_2$C > Cr–N$_4$–Gr/V$_2$C > Mn–N$_4$–Gr/V$_2$C > Cu–N$_4$–Gr/V$_2$C, with the results ranging from −5.64 to −1.59 eV.

The transition metal d-band center is a useful parameter for predicting the catalytic performance of a catalyst. The calculated d-band center (d_ε) is shown in Fig. 2, and the results indicate that the d_ε of Ti–N$_4$–Gr/V$_2$C, Cr–N$_4$–Gr/V$_2$C, and Mn–N$_4$–Gr/V$_2$C are close to the Fermi level (E_f). The absorption would, therefore, be too strong for the intermediate and may deactivate the catalyst. In addition, the d_ε of Cu–N$_4$–Gr/V$_2$C and Zn–N$_4$–Gr/V$_2$C are far from the E_f, resulting in an adsorption capacity too weak for the ORR. Unlike Ti-, Cr-, Mn-, and Cu-based systems, Fe-, Ni-, and Co-based systems have moderate d_ε values and are expected to show good catalytic activity for the ORR.

3.1   ORR thermodynamic process of the M–N$_4$–Gr/V$_2$C heterojunction catalyst

Due to the weak adsorption of O$_2$ and *OOH on pristine graphene and transition metal atom-doped graphene, such as M–
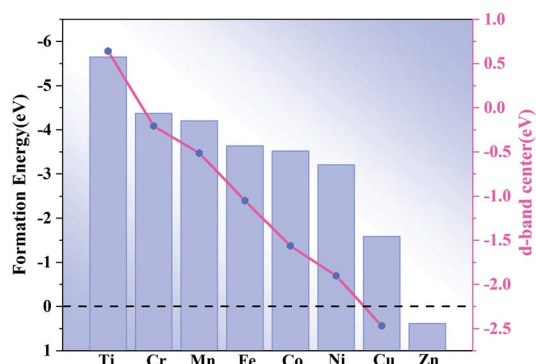
Fig. 2 Formation energy and d-band center of different transition metal heterostructures M–N$_4$–Gr/V$_2$C (M = Ti, Cr, Mn, Fe, Co, Ni, Cu, and Zn).

N–Gr, the ORR always *via* the associative mechanism rather than the dissociative mechanism. ORR needs to overcome the high energy barrier on the surface.[44–46] Therefore, in our calculations, we calculated the catalytic activity of M–N$_4$–Gr/V$_2$C using the binding pathway of ORR (eqn (3)–(6)). To understand the catalytic effect of the M–N$_4$–Gr/V$_2$C catalyst, we calculated the thermodynamic processes to obtain the Gibbs free energy of the 4e$^-$ path at $U = 0$ and 1.23 V as well as the theoretical voltage to evaluate the catalytic performance of the M–N$_4$–Gr/V$_2$C catalyst. It should be noted that the overpotential (η^{*ORR}) for the assessment of catalytic activity is determined by the maximum free energy difference (ΔG) in the 4e$^-$ step, indicating that a lower free energy may not always lead to better catalytic

performance. The ORR process for Ti–N$_4$–Gr/V$_2$C, Cr–N$_4$–Gr/V$_2$C, and Mn–N$_4$–Gr/V$_2$C had high overpotentials, resulting in poor catalytic activity, while the η^{*ORR} values of Fe–N$_4$–Gr/V$_2$C, Co–N$_4$–Gr/V$_2$C, Ni–N$_4$–Gr/V$_2$C, and Cu–N$_4$–Gr/V$_2$C were relatively low at 0.69, 0.45, 0.32, and 0.50 V, respectively. As shown in Fig. 3, at an electrode potential of zero ($U = 0$ V), the free energies of the basic reduction steps for the Mn–N$_4$–Gr/V$_2$C, Fe–N$_4$–Gr/V$_2$C, Co–N$_4$–Gr/V$_2$C, Ni–N$_4$–Gr/V$_2$C, and Cu–N$_4$–Gr/V$_2$C catalysts and their theoretical potentials decreased, indicating that the ORR process was self-initiated. Experimental and theoretical calculations have revealed that changes in the adsorption of oxygen-containing intermediates are key to rate limiting in catalytic reactions.[47] The hydrogenation of OH to water increased significantly in the Ti–N$_4$–Gr/V$_2$C and Cr–N$_4$–Gr/V$_2$C catalysts, which is not favorable for the ORR process. The hydrogenation *OH to H$_2$O is the rate-determining step for Ti–N$_4$–Gr/V$_2$C, Cr–N$_4$–Gr/V$_2$C, Mn–N$_4$–Gr/V$_2$C, Fe–N$_4$–Gr/V$_2$C, Co–N$_4$–Gr/V$_2$C, Ni–N$_4$–Gr/V$_2$C, and Cu–N$_4$–Gr/V$_2$C. Among them, Ni–N$_4$–Gr/V$_2$C and Co–N$_4$–Gr/V$_2$C exhibited high ORR performance with theoretical overpotentials of 0.32 and 0.45 V, respectively; Co–N$_4$–Gr/V$_2$C showed a catalytic activity comparable to that of the Pt/C catalyst.

The free energy of adsorption of oxygen-containing intermediates of ORR is shown in Table 2. The results showed that the free energies of adsorption of O on Ti–N$_4$–Gr/V$_2$C (-1.67 eV) and Cr–N$_4$–Gr/V$_2$C (-0.01 eV) were significantly lower than on the other reactive groups (1.65–2.75 eV). As mentioned above, the strong binding of O prevents the subsequent reaction process. This is illustrated in the energy diagram in Fig. 3a,
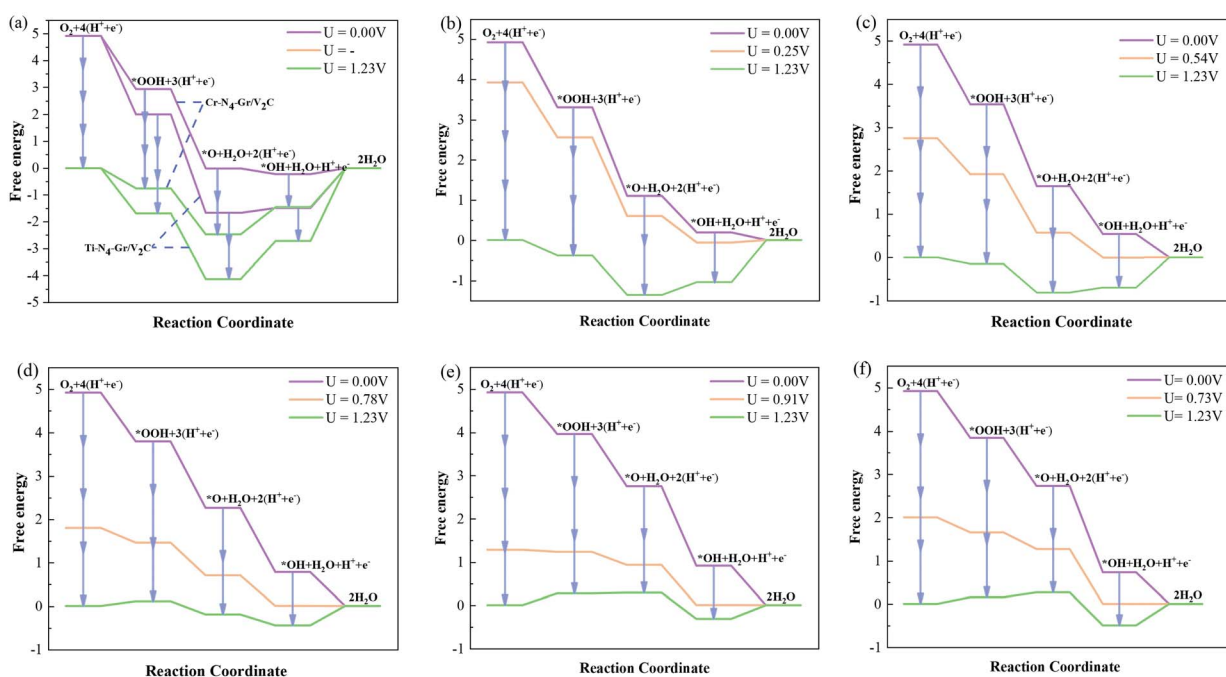

Fig. 3 Free energy diagrams of ORR intermediates on (a) Ti–N$_4$–Gr/V$_2$C, Cr–N$_4$–Gr/V$_2$C, (b) Mn–N$_4$–Gr/V$_2$C, (c) Fe–N$_4$–Gr/V$_2$C, (d) Co–N$_4$–Gr/V$_2$C, (e) Ni–N$_4$–Gr/V$_2$C, and (f) Cu–N$_4$–Gr/V$_2$C surfaces at zero electrode potential (purple lines), working potential (orange lines), and equilibrium potential (green lines).
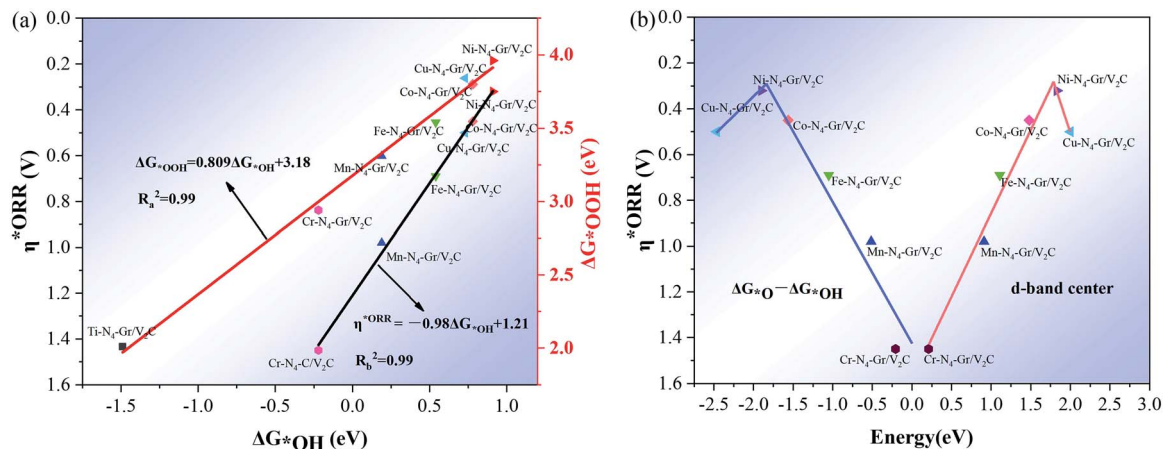
Fig. 4 (a) Scaling relationships of OOH (ΔG_{*OOH}) in proportion to the adsorption free energy of OH (ΔG_{*OH}) and the overpotential η^{*ORR} in proportion to OH (ΔG_{*OH}); (b) volcano plot of η^{*ORR} versus the change in Gibbs free energy ($\Delta G_{*O} - \Delta G_{*OH}$) and η^{*ORR} versus d-band center curves.

where the rate-determining steps of the ORR on M–N$_4$–Gr/V$_2$C are the generation of *OH and *OOH from *O.

The linear relationship of the Gibbs free energy between different oxygen-containing intermediates was obtained during the calculation of the 4e$^-$ reaction, further revealing the performance of ORR on these heterogeneous structured catalysts. As shown in Fig. 4a, a strong linear relationship exists between the oxygenated intermediate *OOH (G_{*OOH}) and *OH (ΔG_{*OH}) Gibbs free energies, center as descriptors, where the Ni–N$_4$–Gr/V$_2$C catalyst is located at the top of the volcano plot and demonstrates the highest activity. A comparison with the corresponding data on the Pt(111) surface revealed that Ni–N$_4$–Gr/V$_2$C has a high catalytic performance for ORR. The d-band center revealed improved catalytic activity between −1.5 and −2.5, with Ni–N$_4$–Gr/V$_2$C showing the highest catalytic activity.

3.2 Effect of V$_2$C as the substrate material on M–N$_4$–Gr

To study the effect of V$_2$C as a substrate carrier material on M–N$_4$–Gr, we calculated the projected DOS (Fig. 5). In the absence of V$_2$C as the substrate material, Ti–N$_4$–Gr and Cr–N$_4$–Gr catalysts exhibit a small amount of electron crossing at the Fermi energy level and possess significant electron leaps at the Fermi energy level, indicating their very weak conductivity.

Notably, Ni–N$_4$–Gr exhibits semiconducting properties through its paramagnetism, a perfectly symmetric electron population in the spin-up and spin-down orbitals, and lack of an electron leap at the Fermi energy level. However, in the presence of V$_2$C substrate as the material (Fig. S1†), the M–N$_4$–Gr/V$_2$C catalyst undergoes a large number of electron transitions at both Fermi energy levels, while Ni–N$_4$–Gr changes from paramagnetic to the metallic nature of Ni–N$_4$–Gr/V$_2$C with strong electron transfer ability. This further indicates that V$_2$C as the carrier material can improve the conductivity of the catalyst and thus the catalytic activity. Moreover, the Bader charges of the transition metals with and without the V$_2$C base material were calculated. In the absence of V$_2$C, M experiences losses in charge transfer to N in M–N$_4$–Gr, while this charge loss

gradually decreases with the change of M. The charge transfer range is 1.66–0.86e. In the presence of V$_2$C as the substrate material, the charge transfer of M in M–N$_4$–Gr/V$_2$C decreased significantly to 1.39–0.61e (Table S1†), indicating that the adsorption is favored when oxygen-containing intermediates are adsorbed, further facilitating the catalytic reactions.

3.3 Effects of changes in electronic structure on ORR activity

The adsorption of reactants on the catalyst surface is a prerequisite for the ORR. We investigated the adsorption properties of oxygen-containing intermediates on different transition metal surfaces. Table 3 shows the adsorption energy of O$_2$ (E_{ads-O_2}), the distance between adsorbed oxygen atom (d_{O-O}), the distance between transition metal and oxygen atoms (d_{M-O}), and the number of charges obtained by O$_2$ from M–N$_4$–Gr/V$_2$C ($Q - O_2$). The adsorption energy and O–O bond length of O$_2$ were in the ranges of −0.46 to −4.25 eV and 1.28 to 0.46 Å, respectively, indicating its ability to adsorb stably on the surface. In the reaction process, the binding of an effective catalytic site to an intermediate cannot be too strong or it would be not conducive to further reduction reactions. After the stabilization of O$_2$ adsorption, the O–O bond lengths were measured and were found to all be elongated compared to the bond length of O$_2$ itself (1.21 Å). In addition, O$_2$ and *OOH got different charges from the transition metal M, and the corresponding charge transfer ranges were 0.39–0.97e and 0.49–0.58e, respectively, and it can be found that O$_2$ and *OOH at Ni–N$_4$–Gr/V$_2$C from M get the least charge, indicating that they are relatively weakly adsorbed on the surface and can be desorbed in the reaction, which is favorable for the ORR reaction. O$_2$ possessed different charges, mainly due to charge transfer from the MN$_4$ group to O$_2$, indicating that the M–N$_4$ group was the active center.

The electronic properties of O$_2$ adsorbed on the M–N$_4$–Gr/V$_2$C catalysts were calculated to reveal the high reactivity and ORR activity of the constructed heterostructure catalysts. First, the partial density of states (PDOS) of all catalysts were found to exhibit strong DOS at the Fermi energy level (E_f), and the M-
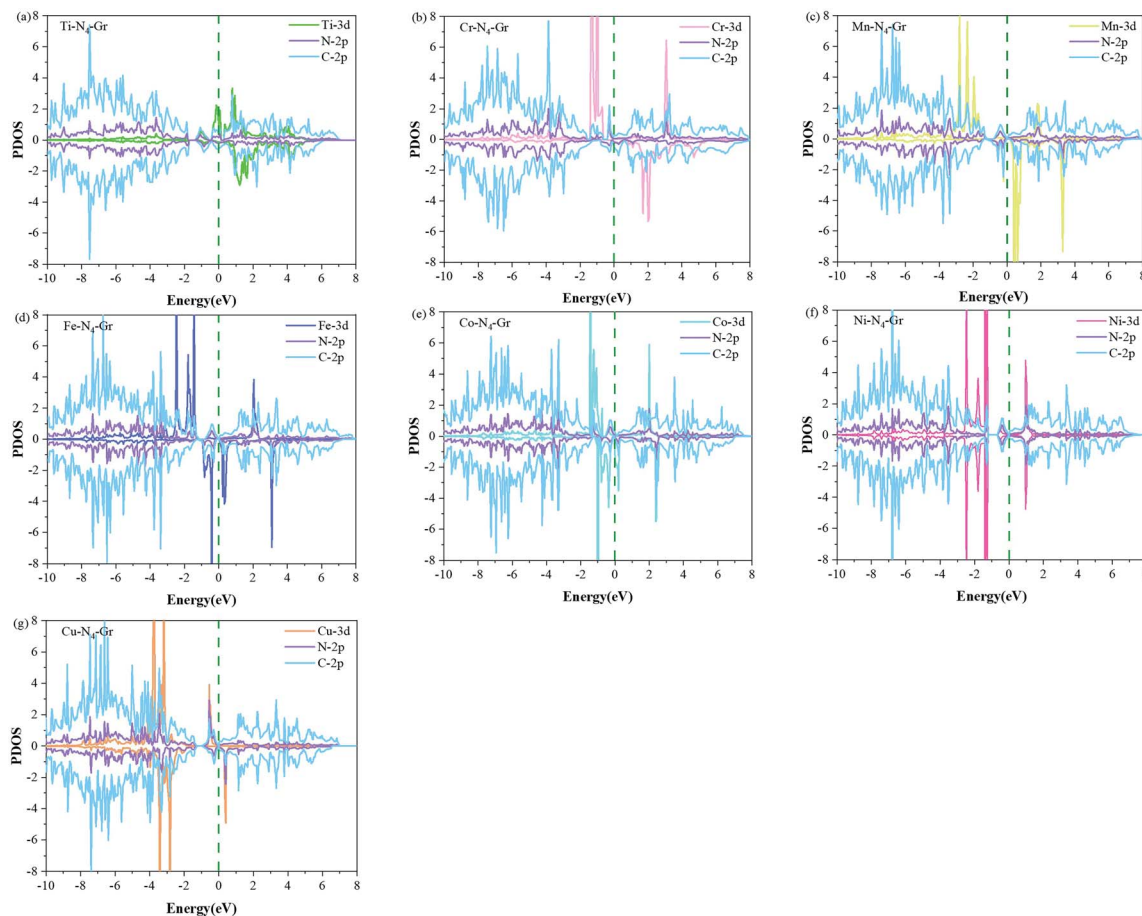
Fig. 5 PDOS plots of M-3d, N-2p, and C-2p for (a–g) M–N$_4$–C (M = Ti, Cr, Mn, Fe, Co, Ni, and Cu). The dotted line at zero represents the Fermi energy level.

Table 3 Adsorption energy of oxygen (E_{ads-O_2}), intermolecular distance of adsorbed oxygen (d_{O-O}), distance between transition metal and O atoms (d_{M-O}), number of charge transfers obtained by O$_2$ ($Q - O_2$) and OOH ($Q - OOH$ (e)) from the M–N$_4$–Gr/V$_2$C substrate ($Q - O_2$)

Properties	E_{ads-O_2} (eV)	d_{O-O} (Å)	d_{M-O} (Å)	$Q - O_2$ (e)	$Q - OOH$ (e)
Ti–N$_4$–Gr/V$_2$C	−4.25	1.46	1.75	0.97	0.56
Cr–N$_4$–Gr/V$_2$C	−2.16	1.42	1.68	0.85	0.57
Mn–N$_4$–Gr/V$_2$C	−1.17	1.42	1.83	0.86	0.83
Fe–N$_4$–Gr/V$_2$C	−0.90	1.30	1.93	0.51	0.52
Co–N$_4$–Gr/V$_2$C	−0.53	1.29	2.08	0.56	0.51
Ni–N$_4$–Gr/V$_2$C	−0.46	1.28	2.14	0.39	0.49
Cu–N$_4$–Gr/V$_2$C	−0.71	1.29	1.95	0.43	0.53

d orbitals were strongly coupled to the O-p orbitals, indicating the high M-3d electron concentration within the catalyst (Fig. S2†). These high 3d states provided enough electrons for the intermediates, which led to extremely strong interactions and the difficult release of the intermediates. In contrast, the Co–N$_4$–Gr/V$_2$C and Ni–N$_4$–Gr/V$_2$C catalysts showed marked improvement with moderate binding compared to the other catalysts. The Co-3d and Ni-3d states not only had significant

peak overlap with the O-2p orbitals at the Fermi energy level (Fig. 6) but also have moderate interactions at the catalyst and intermediate. Second, in the analysis of the distribution of exchange charges, the charge on the substrate gradually decreases, transferring to the transition metal and further transferring to the O$_2$ molecule. As shown in Table 3, the O$_2$ molecule gains a significant amount of charge, making it easier for O$_2$ to adsorb on the catalyst, with a charge transfer range of 0.39–0.97e. Meanwhile, the O–O bond length is significantly stretched compared to the initial length of 1.21 Å, indicating the favored reduction of O$_2$. Finally, for O$_2$ adsorbed in the Co–N$_4$–Gr/V$_2$C and Ni–N$_4$–Gr/V$_2$C distributions of exchange charges (Fig. 6a and b insets), the blue and yellow regions represent the depletion and accumulation of electrons, respectively. The differences in charge density indicate that the positive charges are mainly concentrated in the middle of the two O atoms perpendicular to the O–O bond, while the negative charges are mainly concentrated on the two O atoms, leading to repulsive interactions between them.[48] In general, the negative charge accumulated on the O atom helps to trigger the dissociation of O$_2$. O$_2$ molecules receive their charge from the M–N$_4$ group, which is considered as the reactive group, and its electron donating capacity is a key factor affecting the catalytic activity of the system.
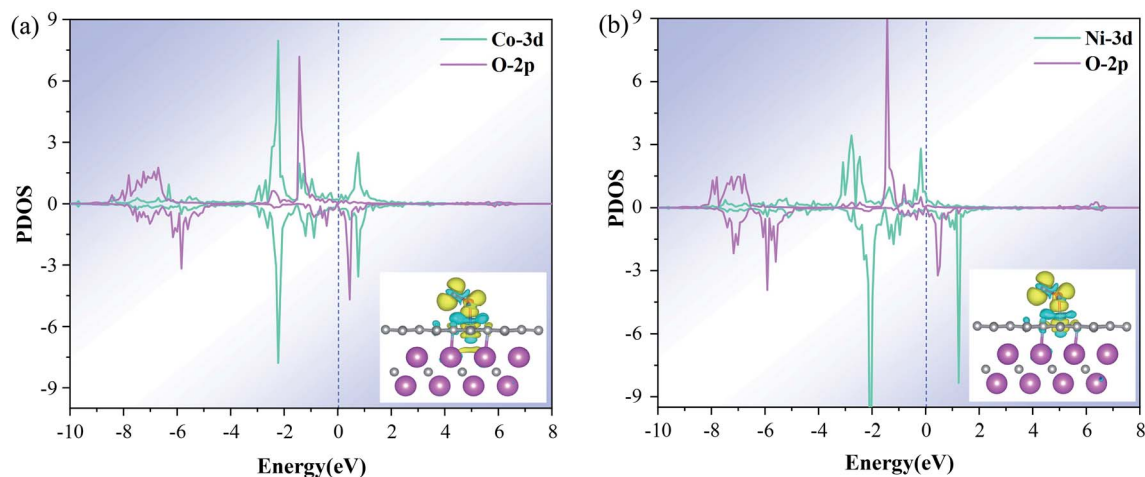
Fig. 6 PDOS of O_2 adsorbed on (a) Co−N$_4$−Gr/V$_2$C and (b) Ni−N$_4$−Gr/V$_2$C catalysts with M 3d and O 2p. The inset is the difference charge density between O_2 and Co−N$_4$−Gr/V$_2$C or Ni−N$_4$−Gr/V$_2$C with an isovalue of 0.054e Å^{-3}. The blue and yellow bubbles represent positive and negative charges, respectively.
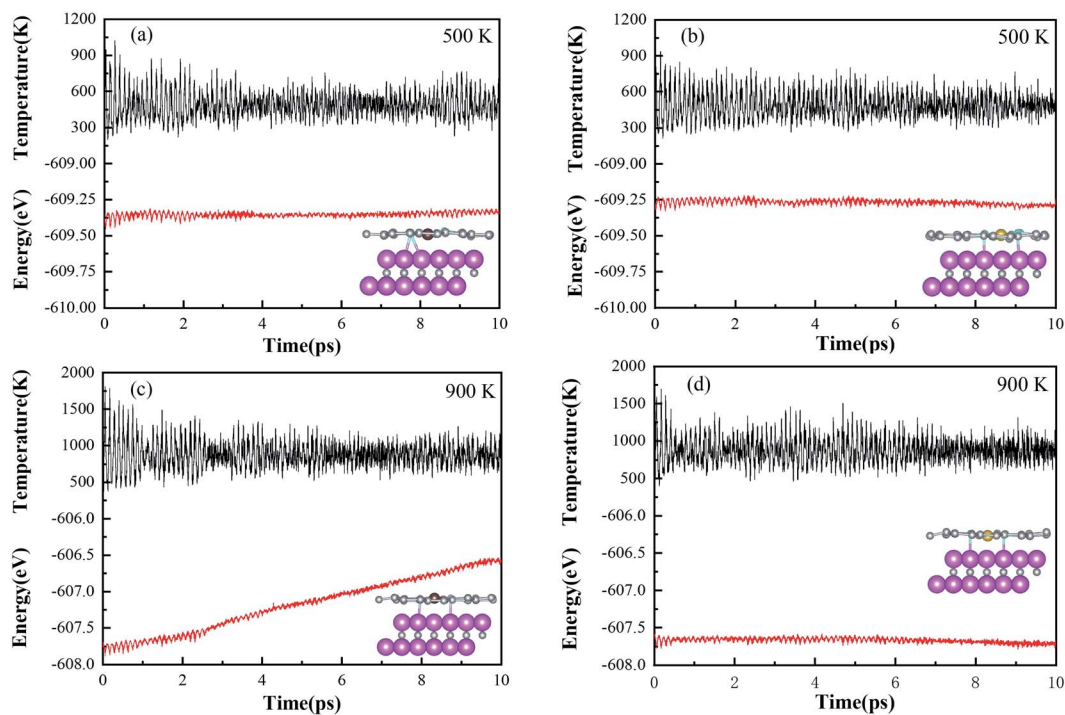

Fig. 7 Change in total energy of the Co−N$_4$−Gr/V$_2$C catalyst after 10 ps of MD simulation at (a) 500 K and (c) 900 K. Change in total energy of the Ni−N$_4$−Gr/V$_2$C catalyst after 10 ps of MD simulation at (b) 500 K and (d) 900 K.

The designed Ni−N$_4$−Gr/V$_2$C and Co−N$_4$−Gr/V$_2$C catalysts were subjected to dynamics testing (Fig. 7). The results showed that the energy of the Ni−N$_4$−Gr/V$_2$C catalyst oscillated back and forth over a range and no bonds were broken or formed between the atoms during the simulation, indicating that the Ni−N$_4$−Gr/V$_2$C catalyst was kinetically stable. In contrast, the Co−N$_4$−Gr/V$_2$C catalyst showed significant energy fluctuations at 900 K, which may destabilize the catalyst.

4 Conclusion

We simulated the heterostructures of eight different transition metals (M = Ti, Cr, Mn, Fe, Co, Ni, Cu, and Zn) doped with nitrogen-coordinated graphene with V$_2$C as potential ORR catalysts using DFT calculations and investigated the heterostructure stability, active volcano map, electrical conductivity, adsorption energy of the intermediates, and electronic structure

of the transition metals. It was found that the heterostructure catalysts were thermodynamically stable, except for Zn–N_4–Gr/V_2C. Moreover, it was thermodynamically determined that Ni–N_4–Gr/V_2C is a potential ORR catalyst with an overpotential of 0.32 V, and the d-band center as a descriptor has a good volcano curve relationship with the overpotential. In the presence of the V_2C substrate, there is a strong electron jump at the Fermi energy level, improving the conductivity of the catalyst. The Ni–N_4–Gr/V_2C catalysts also demonstrated excellent thermodynamic stability at 500 and 900 K. The results are significant for the rational design of transition metal-doped N-liganded graphene/MXene heterostructure catalysts with high ORR performance.

Author contributions

Yunjian Chen: conceptualization, data curation, formal analysis, investigation, methodology, software, visualization. Qi Jiang: investigation. Xue Bai: formal analysis, project administration, supervision. Pengyue Shan: supervision, visualization. Tong Liu: investigation, project administration, writing – review & editing. Yazhou Wang: resources, writing – original draft. Hong Cui: funding acquisition, resources, supervision, writing – review & editing. Rong Feng: supervision, validation. Qin Kang: supervision, validation. Zhiyong Liang: supervision, validation. Hongkuan Yuan: resources, software. All authors have given their approval to the final version of the manuscript.

Conflicts of interest

There are no conflicts to declare.

Acknowledgements

References

1 A. Nouri-Khorasani, A. Bonakdarpour, B. Fang and D. P. Wilkinson, *ACS Appl. Mater. Interfaces*, 2022, **14**, 9084–9096.

2 L. Lu, B. Wang, D. Wu, S. Zou and B. Fang, *Nanoscale*, 2021, **13**, 3709–3722.

3 B. C. H. Steele and A. Heinzel, *Nature*, 2001, **414**, 345–352.

4 J. Snyder, T. Fujita, M. W. Chen and J. Erlebacher, *Nat. Mater.*, 2010, **9**, 904–907.

5 B. Fang, L. Daniel, A. Bonakdarpour, R. Govindarajan, J. Sharman and D. P. Wilkinson, *Small*, 2021, **17**, 2102288.

6 M. Naguib, V. N. Mochalin, M. W. Barsoum and Y. Gogotsi, *Adv. Mater.*, 2014, **26**, 992–1005.

7 B. Anasori, M. R. Lukatskaya and Y. Gogotsi, *Nat. Rev. Mater.*, 2017, **2**, 16098.

8 S. J. Kim, H.-J. Koh, C. E. Ren, O. Kwon, K. Maleski, S.-Y. Cho, B. Anasori, C.-K. Kim, Y.-K. Choi, J. Kim, Y. Gogotsi and H.-T. Jung, *ACS Nano*, 2018, **12**, 986–993.

9 E. Lee, A. VahidMohammadi, Y. S. Yoon, M. Beidaghi and D.-J. Kim, *ACS Sens.*, 2019, **4**, 1603–1611.

10 Y. Ma, N. Liu, L. Li, X. Hu, Z. Zou, J. Wang, S. Luo and Y. Gao, *Nat. Commun.*, 2017, **8**, 1207.

11 Z. W. Seh, K. D. Fredrickson, B. Anasori, J. Kibsgaard, A. L. Strickler, M. R. Lukatskaya, Y. Gogotsi, T. F. Jaramillo and A. Vojvodic, *ACS Energy Lett.*, 2016, **1**, 589–594.

12 Z. Li and Y. Wu, *Small*, 2019, **15**, 1804736.

13 J. Zhang, Y. Zhao, X. Guo, C. Chen, C.-L. Dong, R.-S. Liu, C.-P. Han, Y. Li, Y. Gogotsi and G. Wang, *Nat. Catal.*, 2018, **1**, 985–992.

14 X. Wu, Z. Wang, M. Yu, L. Xiu and J. Qiu, *Adv. Mater.*, 2017, **29**, 1607017.

15 Z. Zhang, H. Li, G. Zou, C. Fernandez, B. Liu, Q. Zhang, J. Hu and Q. Peng, *ACS Sustainable Chem. Eng.*, 2016, **4**, 6763–6771.

16 L. Jiang, J. Duan, J. Zhu, S. Chen and M. Antonietti, *ACS Nano*, 2020, **14**, 2436–2444.

17 B. Wei, Z. Fu, D. Legut, T. C. Germann, S. Du, H. Zhang, J. S. Francisco and R. Zhang, *Adv. Mater.*, 2021, **33**, 2102595.

18 Q. Peng, J. Zhou, J. Chen, T. Zhang and Z. Sun, *J. Mater. Chem. A*, 2019, **7**, 26062–26070.

19 Y. Xie, C. Zhang, X. He, J.-W. Su, T. Parker, T. White, M. Griep and J. Lin, *Appl. Surf. Sci.*, 2019, **464**, 344–350.

20 Y. Xie, C. Zhang, J.-W. Su, H. Deng, C. Zhang and J. Lin, *ChemSusChem*, 2019, **12**, 473–479.

21 A. Kumar, S. Ibraheem, T. Anh Nguyen, R. K. Gupta, T. Maiyalagan and G. Yasin, *Coord. Chem. Rev.*, 2021, **446**, 214122.

22 X. Zhang, J. Lei, D. Wu, X. Zhao, Y. Jing and Z. Zhou, *J. Mater. Chem. A*, 2016, **4**, 4871–4876.

23 P. Li, J. Zhu, A. D. Handoko, R. Zhang, H. Wang, D. Legut, X. Wen, Z. Fu, Z. W. Seh and Q. Zhang, *J. Mater. Chem. A*, 2018, **6**, 4271–4278.

24 J. Qu, J. Xiao, H. Chen, X. Liu, T. Wang and Q. Zhang, *Chin. J. Catal.*, 2021, **42**, 288–296.

25 J. Zhou, G. Liu, Q. Jiang, W. Zhao, Z. Ao and T. An, *Chin. J. Catal.*, 2020, **41**, 1633–1644.

26 S. Shen, Z. Wang, Z. Lin, K. Song, Q. Zhang, F. Meng, L. Gu and W. Zhong, *Adv. Mater.*, 2022, **34**, 2110631.

27 Z. Wang, B. Xiao, Z. Lin, Y. Xu, Y. Lin, F. Meng, Q. Zhang, L. Gu, B. Fang and S. Guo, *Angew. Chem.*, 2021, **133**, 23576–23581.

28 D. Geng, X. Zhao, Z. Chen, W. Sun, W. Fu, J. Chen, W. Liu, W. Zhou and K. P. Loh, *Adv. Mater.*, 2017, **29**, 1700072.

29 S. Zhou, X. Yang, W. Pei, N. Liu and J. Zhao, *Nanoscale*, 2018, **10**, 10876–10883.

30 D. U. Lee, P. Xu, Z. P. Cano, A. G. Kashkooli, M. G. Park and Z. Chen, *J. Mater. Chem. A*, 2016, **4**, 7107–7134.

31 Y. Nie, L. Li and Z. Wei, *Chem. Soc. Rev.*, 2015, **44**, 2168–2201.

32 J. Deng, P. Ren, D. Deng, L. Yu, F. Yang and X. Bao, *Energy Environ. Sci.*, 2014, **7**, 1919–1923.

33 M. Naguib, J. Halim, J. Lu, K. M. Cook, L. Hultman, Y. Gogotsi and M. W. Barsoum, *J. Am. Chem. Soc.*, 2013, **135**, 15966–15969.

34 H. He, Q. Xia, B. Wang, L. Wang, Q. Hu and A. Zhou, *Chin. Chem. Lett.*, 2020, **31**, 984–987.

35 G. Kresse and J. Furthmüller, *Phys. Rev. B: Condens. Matter Mater. Phys.*, 1996, **54**, 11169–11186.

36 J. P. Perdew, K. Burke and M. Ernzerhof, *Phys. Rev. Lett.*, 1996, **77**, 3865–3868.

37 G. Kresse and D. Joubert, *Phys. Rev. B: Condens. Matter Mater. Phys.*, 1999, **59**, 1758–1775.

38 S. Grimme, J. Antony, S. Ehrlich and H. Krieg, *J. Chem. Phys.*, 2010, **132**, 154104.

39 G. Henkelman, A. Arnaldsson and H. Jónsson, *Comput. Mater. Sci.*, 2006, **36**, 354–360.

40 G. Henkelman, B. P. Uberuaga and H. Jónsson, *J. Chem. Phys.*, 2000, **113**, 9901–9904.

41 M. Elstner, D. Porezag, G. Jungnickel, J. Elsner, M. Haugk, T. Frauenheim, S. Suhai and G. Seifert, *Phys. Rev. B: Condens. Matter Mater. Phys.*, 1998, **58**, 7260–7268.

42 J. K. Nørskov, J. Rossmeisl, A. Logadottir, L. Lindqvist, J. R. Kitchin, T. Bligaard and H. Jónsson, *J. Phys. Chem. B*, 2004, **108**, 17886–17892.

43 H. J. Monkhorst and J. D. Pack, *Phys. Rev. B: Solid State*, 1976, **13**, 5188–5192.

44 Y. Yang, K. Li, Y. Meng, Y. Wang and Z. Wu, *New J. Chem.*, 2018, **42**, 6873–6879.

45 X. Xiong, Y. Li, Y. Jia, Y. Meng, K. Sun, L. Zheng, G. Zhang, Y. Li and X. Sun, *Nanoscale*, 2019, **11**, 15900–15906.

46 H. Xu, D. Wang, P. Yang, A. Liu, R. Li, Y. Li, L. Xiao, J. Zhang and M. An, *Phys. Chem. Chem. Phys.*, 2020, **22**, 28297–28303.

47 Z. Wang, S. Shen, Z. Lin, W. Tao, Q. Zhang, F. Meng, L. Gu and W. Zhong, *Adv. Funct. Mater.*, 2022, 2112832.

48 A. Staykov, D. Derekar and K. Yamamura, *Int. J. Quantum Chem.*, 2016, **116**, 1486–1492.